APL Photonics

RESEARCH ARTICLE | MAY 30 2024

778.1 nm distributed feedback lasers for Rb two-photon atomic systems with sub-4 kHz linewidths

E. Di Gaetano ; B. Keliehor; K. Gallacher ; P. F. Griffin ; M. Sorel ; E. Riis ; D. J. Paul

APL Photonics 9, 056114 (2024)
https://doi.org/10.1063/5.0191088

778.1 nm distributed feedback lasers for Rb two-photon atomic systems with sub-4 kHz linewidths

Cite as: APL Photon. 9, 056114 (2024); doi: 10.1063/5.0191088
Submitted: 11 December 2023 • Accepted: 13 May 2024 •
Published Online: 30 May 2024

E. Di Gaetano,[1,a)] B. Keliehor,[2] K. Gallacher,[1] P. F. Griffin,[2] M. Sorel,[1,3] E. Riis,[2] and D. J. Paul[1]

AFFILIATIONS

[1] University of Glasgow, James Watt School of Engineering, Glasgow G12 8LT, United Kingdom
[2] Department of Physics, University of Strathclyde, Glasgow G4 0NG, United Kingdom
[3] Sant'Anna School of Advanced Studies, Via Moruzzi 1, 56124 Pisa, Italy

[a)] **Author to whom correspondence should be addressed:** Eugenio.DiGaetano@glasgow.ac.uk

ABSTRACT

A new epitaxial layer design with a double mode expander layer, high refractive index claddings, and an aluminum-free active area has been used to demonstrate distributed feedback lasers operating at 778.1 nm wavelength with reduced Lorentzian linewidth aimed at miniature atomic clock applications. The design also reduces the vertical beam divergence to improve the modal matching with optical fibers as well as maintain the high power output and reduce the emission linewidth. The lasers demonstrate single-mode operation with an over 35 dB side-mode suppression ratio, a power output ≤58 mW, a coupling efficiency to tapered fibers ≤40%, and a Lorentzian linewidth of 3.7 kHz. The performance allowed the free-running distributed feedback lasers to demonstrate spectroscopy of Rb vapor, which resolved the ^{85}Rb and ^{87}Rb two-photon transitions.

I. INTRODUCTION

Atomic clocks are essential for the function of many areas of modern society, including communications, navigation, logistics, financial trading, and most utility distribution.[1] The atomic clock signal from global satellite navigation system (GNSS) satellites is used as time reference by several productive sectors, such as telecommunication, energy distibution, or transport, however these signals are easy to jam or spoof and are not available indoors, underground, or under the ocean.[2] Therefore, there is a requirement for accurate, field-deployable atomic clocks for a wide range of applications either where GNSS timing is not available or to provide resilience and hold-over if GNSS timing is jammed or spoofed. Chip-scale atomic clocks[3] based on coherent population trapping have allowed for substantial miniaturization, but they have drift resulting in an accuracy of about 1 μs per day, which is too large for many applications.[1] 3U rack mountable Cs beam atomic clocks with an error of ~1 ns per day are therefore used for key applications, but a smaller and cost-effective clock ideally with higher accuracy is highly desirable.[1] Only hydrogen masers or Cs fountain clocks offer better precision commercially at present, but neither are suitable for operation outside environmentally controlled laboratories.

Optical atomic clocks[4] are now being researched, which have the potential to provide higher accuracy than Cs beam clocks but could also be miniaturized[5] using microfabricated components and integrated systems.[6,7] They are less susceptible to environmental conditions than present commercial atomic clocks and primary standards.[1] The stability of an atomic clock is determined by $\frac{\Delta\nu}{\nu}$, where $\Delta\nu$ is the linewidth of the clock optical transition and ν is the frequency of the optical transition in the atom being used. This therefore drives a requirement for compact, narrow-linewidth lasers for atomic clocks. Sr optical atomic clocks have now demonstrated fractional uncertainties below 1 part in 10^{18} and are being investigated as a replacement for the primary standard to replace the present Cs fountain clocks.[8] These optical atomic clocks typically

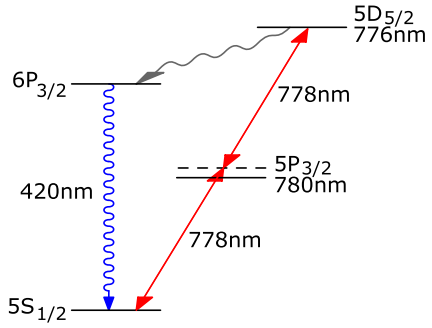

FIG. 1. The energy level diagram of the ^{87}Rb D1 two-photon transition excitation and fluorescence scheme.

require seven different lasers with cold atoms used to produce sub-Hz linewidth atomic transitions and are therefore challenging to miniaturize and mass produce at a low cost.

Rubidium two-photon optical atomic clocks (Fig. 1) are considered to be an option for cost effective, portable, and mass producible optical atomic clocks[5,9] as well as miniature frequency[10,11] and low phase noise oscillators. The linewidth of thermal ^{87}Rb gas at 100 °C from Doppler-free spectroscopy[12,13] is around 334 kHz for an atomic clock transition of 385 THz for the ^{87}Rb $5S_{1/2}(F = 2) \rightarrow 5D_{5/2}$ $(F' = 4)$ two-photon transition (TPT) presented in Fig. 1 with an estimated accuracy of 1 fs (≤1 ns/day) for a clock.[1,9] A compact laser with linewidth <334 kHz is therefore required at a wavelength of 778.1 nm suitable for such miniature Rb two-photon optical atomic clocks.[5] Although 778.1 nm is close enough to 780 nm that the GaAs/AlGaAs technology can support this wavelength, the emission requirements for Rb TPT make this laser device challenging to be realized using the semiconductor technology alone,[14] as the linewidth and stability requirements are comparable to the performance of a solid-state laser.[15] Previous works using a semiconductor laser as a light source for Rb TPT employed either second harmonic generation from a narrow linewidth 1556 nm semiconductor laser[9,16] or an external cavity as stable,[17] but both systems are large and incompatible for full chip-scale integration.

In this work, distributed feedback (DFB) lasers[18,19] emitting at 778.1 nm wavelength are designed, fabricated, and characterized. The laser design aims for high power operation with linewidth <334 kHz and to reshape the device far-field emission pattern in order to maximize the coupling efficiency with optical fibers or photonic integrated circuits.[20,21] An asymmetrical double-sided mode expander layer, embedded into the AlGaAs cladding, has been engineered to reduce the propagation losses and far-field emission pattern and increase the fiber coupling to ≥40%, resulting in a DFB laser emitting ≤58 mW at 778.1 nm with a Lorentzian linewidth of 3.7 kHz. The design incorporates an aluminum-free InGaAsP quaternary active region, allowing higher power density before catastrophic optical damage (COD) or catastrophic optical mirror damage (COMD) compared to AlGaAs active regions.[18,22,23] The DFB laser was employed to spectroscopically probe ^{85}Rb and ^{87}Rb TPT in free running conditions using an acousto-optical modulator (AOM) to scan the frequency. The laser had sufficiently narrow-linewidth to resolve the hyperfine structures for both ^{85}Rb and ^{87}Rb TPTs, proving that it is suitable for use in Rb two-photon atomic

TABLE I. Comparison of narrow-linewidth single mode diode lasers emitting at wavelengths close to Rb TPTs.

	Power (mW)	Linewidth (kHz)	Wavelength (nm)	(θ) (deg)
Kraft *et al.*[14]	80	2000	777.8–781	
Edwards *et al.*[17]	80	1000	778.1	
Ding *et al.*[18]	50	>5000	780.24	
Virtanen *et al.*[24]	28.9	10	780	>40
Nguyen *et al.*[25]	270	35	778.9	
Nguyen *et al.*[26]	80–290	8	782.75–783.5	
Di Gaetano *et al.*[19]	60	612	780.24	
This work	58	3.7	778.1	20.5

systems. The DFB laser produced in this work is also compared in Table I with several semiconductor diode lasers reported in literature emitting in the 775–785 nm range and to the best of our knowledge demonstrates the narrowest reported linewidth from diode lasers at these wavelengths.

II. HETEROSTRUCTURE DESIGN OPTIMIZATION

The laser heterostructure's design is critical for laser properties, such as output wavelength, power, and linewidth, as well as for efficiency in coupling its power into optical fibers or photonic integrated circuits.[20,21] The laser parameters that depend on the transversal modal shape and require to be optimized are as follows: (1) the modal confinement (Γ_{QW}); (2) the material propagation losses (α_{loss}) (i.e., mode propagation loss without considering any surface scattering effect); (3) the far-field distribution, in particular the vertical beam divergence (Θ) defined as the full-width half-maximum (FWHM) of the far-field pattern in the epilayer direction; (4) the grating coupling factor (κ) (i.e., coupling per unit of length); and (5) the transversal modal area $(A_\perp)$ and in turn the average power density in the transversal plane $(P_\perp)$, where the transversal modal area can be defined as $A_\perp = \frac{(\int\int|\phi(x,y)|^2 dxdy)^2}{(\int\int\phi(x,y)|^4 dxdy)}$.[27]

A. Transversal mode guiding

A critical parameter for the transversal modal profile is the shape of the guiding structure. For the considered case of a Bragg grating for a DFB laser, this profile is not constant, but the periodical repetition of two guiding sections, more specifically, a sidewall Bragg grating with grating coupling factor κ, created by the periodical repetition of two ridge waveguides with different widths. The sidewall Bragg grating design will be discussed in detail in this section dedicated to the cavity optimization; however, the inner and outer waveguide widths that define the grating are 1.5 and 2.5 μm, respectively, generating a third-order Bragg grating. To provide a visual representation of the sidewall configuration, a 3D model of a sidewall Bragg grating, defined upon a PIN epilayer structure, is reported in Fig. 2. To take into account the dry etch non-ideality, the ridge waveguide profile was modeled on a real waveguide profile, extracted from the scanning electron microscopy (SEM) picture

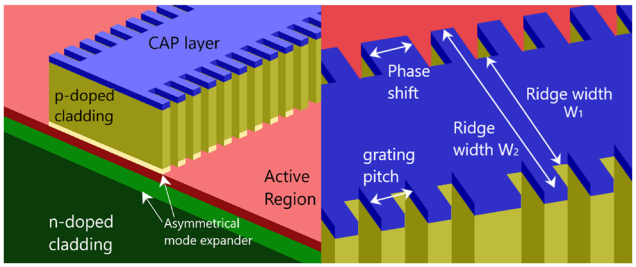

FIG. 2. A 3D model of the sidewall Bragg grating structure in the shallow configuration, realized by limiting the sidewall grating above the active region. The view from the facet prospective is on the left, whereas the lateral view is on the right. The different colors highlight the active region (red), the n-doped cladding (green), the p-doped cladding (yellow), and the CAP layer (blue). The two layers sandwiching the active region represent the asymmetrical mode expander (top side is light yellow; bottom side is light green).

of a previously fabricated laser. Finally, the real waveguide profile is translated into a refractive index profile and transferred into 2D-finite difference eigenmode (FDE) simulation tool Ansys Lumerical.[27] Figure 2 represents the cross section of a ridge waveguide of a sidewall Bragg grating (left) and its translation into the material refractive index (right). The SEM picture clearly demonstrates that the process exhibits a slower etch rate inside the sidewall recess due to the large aspect ratio (i.e., more than 10) of the sidewall Bragg grating.

B. Active region

The entire active area was built using InGaAsP quaternary compounds, which provide the necessary flexibility to generate the required electron and hole band-structures for both quantum wells (QWs) and barriers without aluminum.[19] The full semiconductor band structure of the active area under applied voltage was simulated using an 8-band **k.p** Poisson–Schrödinger solver through the simulation software Nextnano++.[28] The active area, optimized to emit around 778.1 nm under biased, comprises four 4-nm-thick $In_{0.25}Ga_{0.75}As_{0.62}P_{0.38}$ QWs encapsulated between 10-nm-thick $In_{0.24}Ga_{0.76}As_{0.37}P_{0.63}$ barrier layers. The QWs have a compressive strain (1%) over the GaAs substrate lattice constant, allowing the active area to emit selectively in TE polarization, whereas the barrier layers are tensile strained for strain compensation preventing lattice defect relaxation. To inject carriers into the QWs, the active area is then enclosed between two graded separate confinement heterostructure (GRINSCH) layers made by $Al_{1-x}Ga_xAs$ with Al fraction ranging from x = 0.452, matching the band offset of the barriers, to x = 0.481, matching the band offset of the cladding layers. This design is simulated to have a conduction band offset ΔE_C = 1.85 eV, a valence band offset ΔE_V = 0.04 eV, and a current density at transparency J_{th} = 1732 A/cm^2.

C. Mode expander configuration

Following the active region design, the material optimization focused on the design of the mode expander. This is a layer enclosing the active region but surrounded by the $Al_{1-x}Ga_xAs$ cladding, which can be employed to engineer the transversal modal shape. The mode expander is constituted by $Al_{1-x}Ga_xAs$ with x = 0.466, to guarantee enough refractive index contrast with respect to the cladding layer, while it also remains close to the band levels of the GRINSCH layers on both sides of the active region. The two remaining degrees of freedom in the mode expander design are the thickness and center position with respect to the active region defined by the thickness of the top and bottom sides of the mode expander t_{top} and t_{bottom},

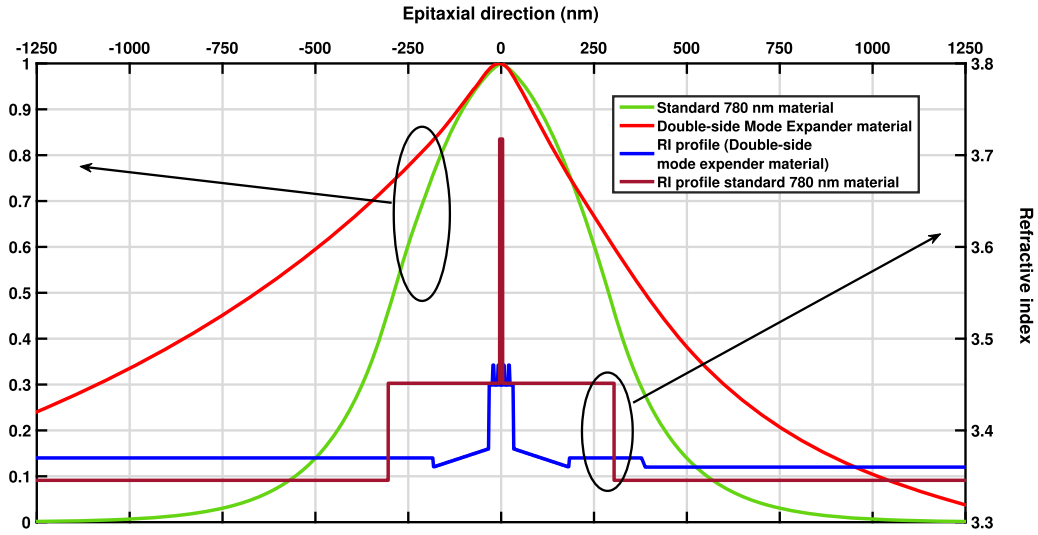

FIG. 3. The refractive index (RI) profile into the active region and the normalized modal field distribution along the epitaxial direction are reported for both the double-sided mode expander and designs without the mode expanders (from Ref. 24) for emission at 778.1 nm. The larger RI contrast between the active area and the cladding in the standard epilayer generates a more confined modal field distribution.

respectively. The electric field and refractive index of the heterolayers were simulated using the 2D-FDE tool in Ansys Lumerical.[27] An example of the double-side mode expander configuration, and its effect on the modal profile, is represented in Fig. 3.

The mode expander pulls the mode outside the active region due to its higher refractive index with respect to the rest of the cladding (Fig. 3). The advantage in having a double-sided mode expander, which extends from both sides of the active region, is a larger flexibility in engineering the transversal modal shape, and in turn the laser parameters, when compared with a single or symmetrical mode expander. The introduction and change in thickness of the top and bottom side of the mode expander t_{top} and t_{bottom} have different, and in some cases opposite, effects on the laser performance parameters depending on the material design. Some parameters, such as Γ_{QW}, are reduced by the mode delocalization outside the active region, whereas other parameters, such as the modal area $A_\perp$, would always increase with mode expansion. Finally, some other parameters, such as propagation losses α_{loss}, can change in either value depending on the direction of the mode expansion. Therefore, the material optimization consists in finding a trade-off configuration for the double-sided mode expander to achieve the parameters required for low Θ, high $P_\perp$, narrow-linewidth (ν_{S-T}), and low current threshold (I_{th}).

Sections II D and II E present the mode expander optimization for the cited laser properties. A detailed and comprehensive analysis of the relationships between the laser parameters and the double-sided mode expander design is provided in the supplementary material.

D. Vertical beam divergence and modal area

The vertical beam divergence, Θ, indirectly depends on the modal profile. For symmetrical epitaxial layer designs, the narrow extension of the multiple-QW active region generates an elliptically shaped transversal mode profile with a larger optical mode in the ridge waveguide direction and a narrower optical mode along the vertical direction. The resulting far-field emission pattern, which can be derived as the spatial Fourier transform of the near-field profile, has an elliptical shape with a narrower optical mode in the horizontal direction.

From 2D-FDE simulations, the best field overlap between the mode profile and the lensed fiber, assuming a 1.2 μm Gaussian beam shape at the beam waist for the lensed fiber, is simulated to be up to 50% if the vertical beam divergence Θ is reduced to 20°, whereas the same is simulated to be ≤28% for beam divergence above 45° (i.e., the condition without the double-sided mode expander). These simulated field overlap values are obtained under ideal conditions, i.e., perfect alignment between components in all directions and angles; therefore, they represent a maximum theoretical limit for the coupling. The relative increase of the coupling value, however, is a good indicator of the coupling improvement under the same alignment conditions. In terms of the vertical beam improvement, the top and bottom sides of the mode expander play an equivalent role as the vertical divergence is proportional to the modal size along the epitaxial layer directly, regardless of the center of the mode profile. An example is provided in Fig. 4 where Θ is plotted for increasing both t_{top} and t_{bottom}, while the other side is kept at zero.

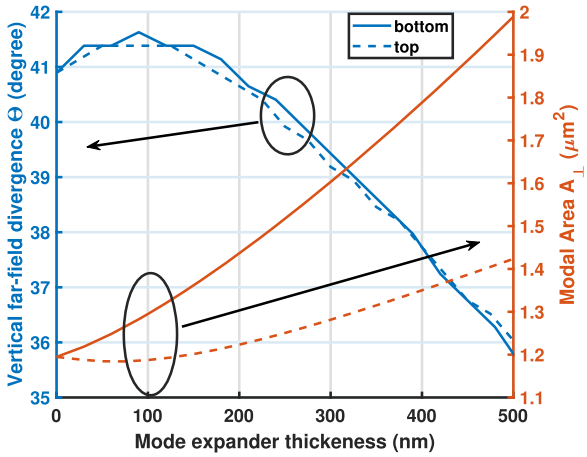

FIG. 4. Θ (left) and $A_\perp$ (right) for increasing thickness t_{bottom} (linear) and t_{top} (dotted), respectively, when the other mode expander side is not present.

The average $P_\perp$ is inversely proportional to the modal area $A_\perp$ for a fixed output power as

$$P_\perp = \frac{P_{out}}{A_\perp}. \tag{1}$$

From an intuitive point of view, an increase in $A_\perp$ should entail a reduction of $P_\perp$ as the same total power is distributed over a larger area. The power density $P_\perp$ is the key parameter for the appearance of COD,[29] COMD,[30] and non-linear effects,[31] as well as the laser lifetime,[32] as these detrimental conditions will start above a certain light intensity rather than total power. Hence, the optimization of $A_\perp$ is beneficial for the laser power output as it allows us to generate a larger power output before reaching this power density threshold. A role similar to $A_\perp$ is played by the cavity length L, although the cavity length is also affecting other cavity properties (e.g., the total cavity feedback κL); this will be further analyzed in the cavity optimization section. The influence on $A_\perp$ of the top and bottom sides of the mode expander is asymmetrical. Figure 4 demonstrates that an increase in t_{bottom} has a larger relevance than the same increase in t_{top}. This behavior is a consequence of the ridge waveguide geometry; the mode has more semiconductor material to expand into when expanded toward the substrate rather than toward the ridge region, hence a larger mode total area. An asymmetrical mode expander configuration can be employed to reflect this uneven effect; as an example, a value of t_{bottom} above 2.5 μm would guarantee $A_\perp$ larger than 3.3 μm^2, regardless of the t_{top} value.

E. Linewidth and threshold current

A narrow intrinsic linewidth is a key property for many quantum applications and especially optical atomic clocks. The natural Lorentzian linewidth ν_{S-T} in semiconductor lasers can be expressed by the Schawlow–Towns formula, which links the contribution due to spontaneous emission to the laser cavity and material parameters[33] through

$$\nu_{S-T} = \frac{K n_{sp} v_g^2 h\nu (\alpha_{loss} + \alpha_m)\alpha_m}{4\pi P_\perp A_\perp}(1 + \alpha_H^2), \tag{2}$$

where α_m are the equivalent mirror losses (derived by the Bragg grating for a DFB laser), α_H is the linewidth enhancement factor,[33] K is the Petermann's factor, v_g^2 is the group velocity, and n_{sp} is the spontaneous emission factor.[25] It is worth noting that the Schawlow–Towns formula has been expressed in terms of average power density $P_\perp$ rather than total output power P_{out} using Eq. (1), as the power density to define the threshold where laser damage from high power takes place. Equation (2) is accurate for Fabry–Pérot feedback, whereas DFB cavities can have a non-uniform power distribution due to the presence of a Bragg grating; nevertheless, the average power density remains a good indicator $P_\perp$ for power level in this analysis. The fabricated laser devices will have antireflection (AR)/high-reflection (HR) coating ($R_{AR} < 0.1\%/R_{HR} > 95\%$); therefore, the Fabry–Pérot feedback from the facet would be heavily reduced and the total feedback dominated by the Bragg grating feedback. As the cavity is designed as a phase-shifted sidewall Bragg grating, the photon density distribution was not analyzed in this work; however, the influence of the photon density on the laser linewidth was detailed in previous work.[34] The other term in Eq. (2), i.e., $h\nu$, does not depend on the material or the cavity design and can therefore be assumed as a fixed term and will not be considered in the following analysis. In order to evaluate the linewidth narrowing due to the double-sided mode expander, a relative linewidth factor can be expressed as

$$\Delta\nu_{S-T} = \frac{\nu^A_{S-T}}{\nu^0_{S-T}} = \frac{n^A_{sp}}{n^0_{sp}}\frac{A^0_\perp}{A^A_\perp}\frac{(\alpha^A_{loss}+\alpha^A_m)\alpha^A_m}{(\alpha^0_{loss}+\alpha^0_m)\alpha^0_m}, \tag{3}$$

with superscript A being the laser parameters for a specific double-sided mode expander configuration with the mode expander and superscript 0 being the parameters without the mode expander. In the expression of Eq. (3), the power density has been assumed to be the same in both configurations and the lasers operating in linear regime, which is an essential condition for the Schawlow–Townes formula [Eq. (2)] to reflect the intrinsic laser linewidth. The value for the relative linewidth factor in Eq. (3) is calculated using the propagation losses $\alpha^{A,0}_{loss}$ and $\Gamma^{A,0}_{QW}$ treated in the supplementary material, whereas the equivalent mirror losses $\alpha^{A,0}_m$ for a Bragg grating are obtained from the oscillation condition for a phase-shifted grating at its Bragg wavelength [Eq. (6)], assuming constant total feedback in the cavity,[35] i.e., $\kappa L = 1$ and

$$\gamma \coth\frac{\gamma L}{2} - (g_{th} + \kappa r_{HR} e^{2i\phi_{HR}}) = 0, \tag{4}$$

where g_{th} is the modal gain, $\gamma^2 = \kappa^2 + g_{th}^2$, and r_{HR} and ϕ_{HR} are the module and phase, respectively, of the Fresnel reflection coefficient for HR coating. A fixed phase $\phi_{HR} = 0$ was assumed for the g_{th} calculation, whereas $r_{HR} = \sqrt{R_{HR}}$. In Eq. (4), g_{th} represents the gain required in the fundamental mode for lasing. At lasing threshold, however, g_{th} has to be equal to the total cavity losses; therefore, α_m is obtained from Eq. (4) as a function of both κ and L. From Eq. (3), $\Delta\nu_{S-T}$ is derived for the considered configurations of the double-sided mode expander in Fig. 5. Figure 5 demonstrates how the presence of the bottom side is beneficial and a thicker t_{bottom} decreases ν_{S-T} of the laser. On the other hand, the top side effect is smaller, but it can increase or decrease ν_{S-T} depending on the bottom mode expander thickness. In general, the best configurations to reduce ν_{S-T} include a double-sided mode expander with a thick bottom side; a reasonable range is for a bottom side thickness t_{bottom} above 2 μm as it guarantees a ν_{S-T} reduction larger than 88% compared with no double-sided mode expander.

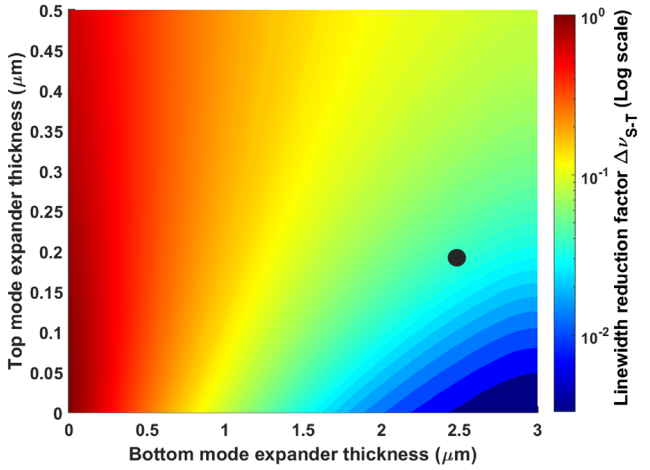

FIG. 5. $\Delta\nu_{S-T}$ as a function of t_{top} and t_{bottom}. The black dot indicates the value used in the final laser design demonstrated experimentally.

The laser threshold current (I_{th}) depends on device properties, such as the contact widths and cavity length;[36] however, the double-sided mode expander effect can be evaluated by a relative threshold current factor (ΔI_{th}) as

$$\Delta I_{th} = \frac{I^A_{th}}{I^0_{th}} = \frac{e^{\frac{\alpha^A_{loss}+\alpha^A_m}{\Gamma^A_{QW} g_0}} - 1}{e^{\frac{\alpha^0_{loss}+\alpha^0_m}{\Gamma^0_{QW} g_0}} - 1}, \tag{5}$$

with g_0 being the gain value for the current density j_0, maximizing the ratio g_0/j_0,[36] which was calculated to be 1266 cm^{-1} for the employed active region. From Eq. (5), the relative threshold current factor ΔI_{th} is obtained and reported in Fig. 6. ΔI_{th} exhibits an increase due to the presence of the bottom side of the

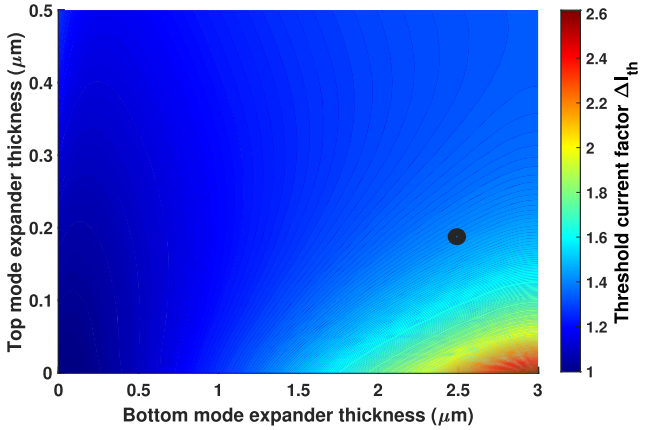

FIG. 6. I_{th} as a function of t_{top} and t_{bottom}. The black dot indicates the value used in the final laser design demonstrated experimentally.

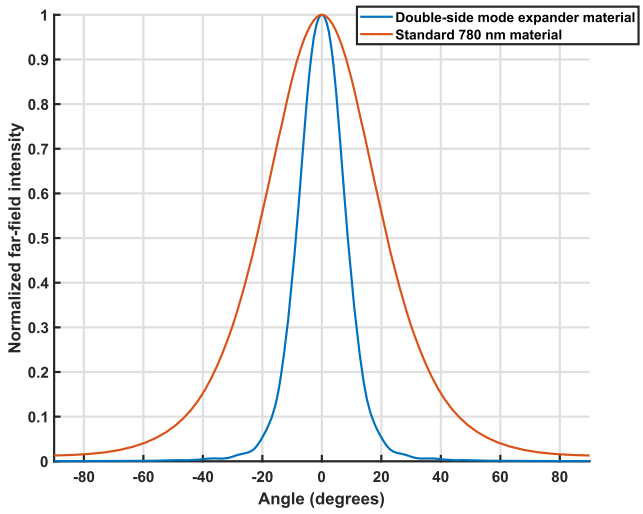

FIG. 7. Θ for an epilayer material without the mode expander (red) and for the optimized asymmetrical mode expander with t_{top} = 0.5 μm and t_{bottom} = 2.5 μm (blue).

mode expander, which can be expected from its effect on α_{loss} and Γ_{QW} (see the supplementary material). The top side of the mode expander tends to mitigate the rise in threshold current due to the bottom side; hence, the top side thickness t_{top} can be suitable to modulate its effect on the threshold current. It is worth noting that the double-sided mode expander configuration favoring linewidth reduction is also increasing the threshold current. This is a consequence of the presence of Γ_{QW} in the opposite sides of Eqs. (3) and (5).

F. Summary

In order to achieve a balance among the considered laser properties, an asymmetrical double-sided mode expander with a top side thickness t_{top} of 0.2 μm and a bottom side thickness t_{bottom} of 2.5 μm is selected. This configuration will benefit several laser properties, such as Θ down to 19.7° with a reduction of 55%, as shown in Fig. 7, and a reduction in v_{S-T} of 20-fold (i.e., 95% reduction) at constant $P_{\perp}$. A drawback of this double-sided mode expander configuration is an increase in the threshold current I_{th} of 28% and a reduction in κ of 56% from 5.6 cm^{-1} without the mode expander to 2.47 cm^{-1} with the mode expander. The summary of the asymmetrical mode expander to the laser parameters is reported in Table II.

III. DFB CAVITY OPTIMIZATION

Following the epilayer material optimization, the geometry and parameter of the DFB cavity are optimized to generate single mode emission, maximize the power output, and narrow the laser linewidth.

A. Bragg grating structure

For simplicity in fabrication, we use a sidewall phase-shifter Bragg grating.[19,34] This sidewall Bragg grating structure can be

TABLE II. Summary comparing the same laser parameters with and without the selected asymmetrical mode expander configuration.

	No. mode expander	Asymmetrical mode expander
Γ_{QW} (%)	4.22	1.29
α_{loss} (cm^{-1})	6.35	4.75
Θ (deg)	45.58	19.7
κ(cm^{-1})	5.6	2.2
$A_{\perp}$ (μm^2)	1.2	5.28
Δv_{S-T}	1	4.1×10^{-2}
ΔI_{th}	1	1.28

defined using two ridge waveguide widths W_1 and W_2, the grating period Λ, and the duty-cycle (i.e., the ratio between W_1 and W_2 along the grating cavity). A higher-order Bragg grating (i.e., third-order grating) was employed to mitigate any fabrication tolerance; hence, the required Bragg grating period Λ for the Bragg condition[37] is

$$\Lambda = m\frac{\lambda_{Bragg}}{2\pi n_{eff}}, \tag{6}$$

where m is the Bragg grating order, n_{eff} is the modal effective index, and λ_{Bragg} is the Bragg wavelength. For an emission wavelength of 778.1 nm, Λ is 351 nm for a third-order Bragg grating, i.e., m = 3, and the material considered in this work. This Bragg grating Λ has been calculated independently from the ridge waveguide width as the effective mode refractive index n_{eff} is mainly dependent on n and changes only marginally with ridge width.

The DFB laser properties considered in the following are simulated as a function of the grating cavity parameters by the 2D-FDE solver, similar to the case of the material parameters. Simulating the effective mode refractive index n_{eff} for the fundamental TE00 mode in a large range of ridge waveguide widths (i.e., from 3 to 1.2 μm, which is larger than the cutoff for first-order mode TE01 and is close to the fundamental mode TE00 cutoff, respectively) exhibits a relative variation as narrow as 2.67×10^{-4} (i.e., $\Delta n_{eff} < 9 \times 10^{-4}$). This effective mode refractive index Δn_{eff} variation is equivalent to less than 0.1 nm in the grating period.

B. Grating ridge waveguides

The periodical variation of ridge waveguide width is employed to generate a refractive index contrast for the guided mode along the longitudinal direction, an essential ingredient to produce a DFB laser. The duty-cycle has been set to a fixed value of 0.5 as this configuration maximizes κ for the employed grating order (i.e., m = 3).[35] A larger value for W_2 would be beneficial in terms of $P_{\perp}$ as it increases $A_{\perp}$, but if too large, then unwanted higher-order modes can be supported. Therefore, a ridge waveguide width W_2 of 2.5 μm is selected as this width is lower than TE01 mode cutoff but still large enough to have some room to play with the width of the inner ridge waveguide W_1. Due to the Reactive Ion Etch (RIE) lag inside the recess, which prevents W_1 being reduced beyond a certain point (see Fig. 8), there is an optimal value of W_1 for κ as narrower W_1 would have a marginal effect and could even be detrimental for

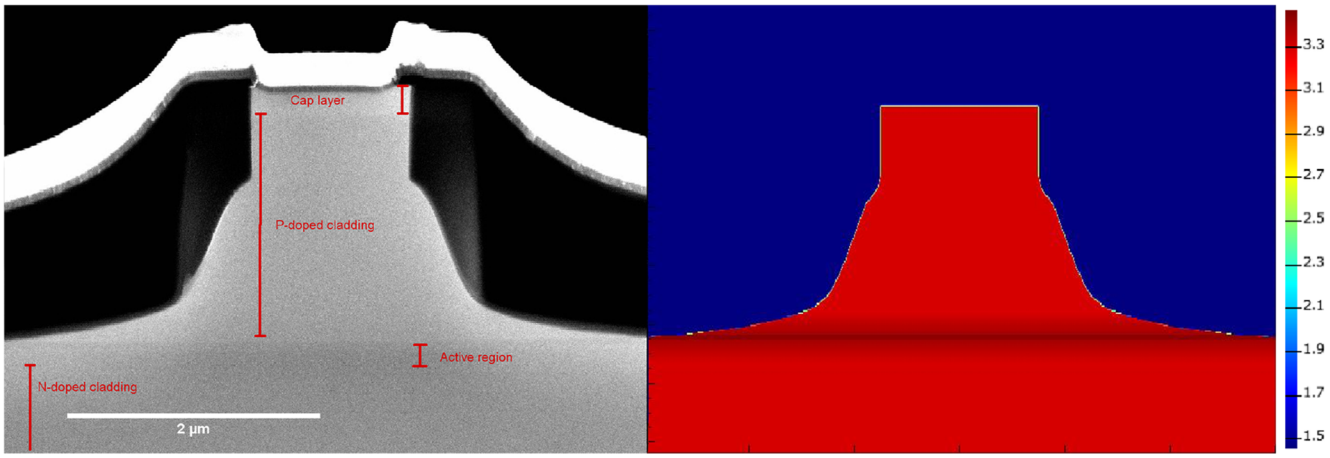

FIG. 8. A SEM image of the cross section for a sidewall Bragg grating (left) compared with the material refractive index profile reconstructed by 2D-FDE Lumerical software (right). The different colors represent the refractive indices of the AlGaAs in red and of the SiO_2 in blue.

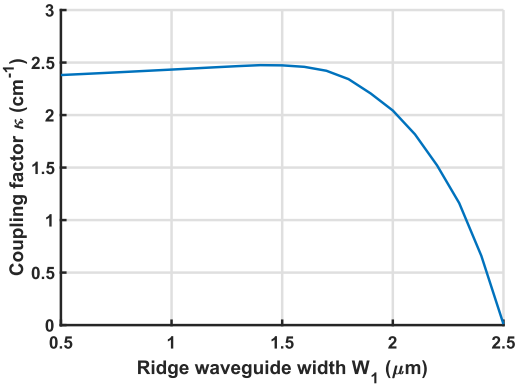

FIG. 9. κ as a function of W_1.

additional RIE lag. κ is simulated using the longitudinally averaged refractive index approximation (see the supplementary material) as a function of W_1 and reported in Fig. 9. Figure 9 shows the expected relationship between κ and W_1 for large values of W_1 because a narrower W_1 translates into a stronger κ. For small values of W_1, however, the effect of the non-ideal profile inside the recess prevails and leads to a change in the relation between W_1 and κ. Therefore, a trade-off value for the inner ridge waveguide W_1 of 1.5 μm can be selected to achieve the largest κ of 2.47 cm^{-1}; this partially compensates for the decrease in κ due to the introduction of the double-sided mode expander in the epitaxial material.

C. Grating cavity length

Longer cavities have larger κL and lower α_m, but this also changes the contact area so that a longer contact implies a larger current to provide the same current density. The cavity length is also important for the power distribution and density inside the laser cavity. Considering the same total power distributed into a ridge waveguide cavity, a longer cavity would have, in general, a smaller power density. Although having a longer cavity does not necessarily translate into the same power density distribution, some grating design strategies can be implemented to control the power distributed along the cavity, as reported in previous work.[34] Moreover, the cavity length would also affect the fraction that can be extracted from the cavity because the ratio between the power output P_{out} and the power inside the cavity is proportional to $\alpha_m L$. In order to assess the effect of the cavity length L on the threshold current I_{th} and laser linewidth ν_{S-T}, the same relative factors from Eqs. (3) and (5) are considered but having the cavity length L as a variable, while the material parameters are kept fixed; in this case, the normalization is performed compared with a cavity length L of 1 mm. Equation (5) also needs to be multiplied by a factor $\frac{L_A}{L_0}$ to take into account the changes to I_{th} due to a longer contact.

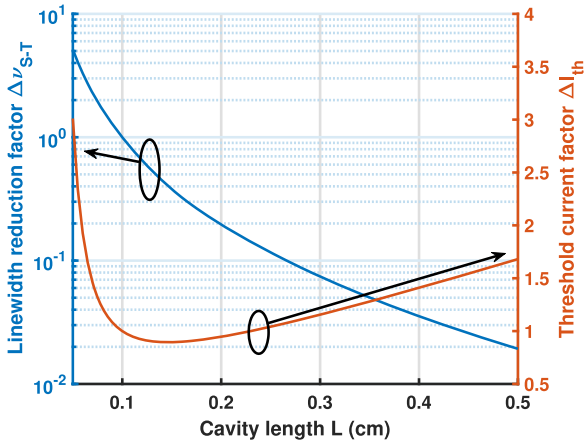

FIG. 10. $\Delta\nu_{S-T}$ (left y axis in logarithmic scale) and ΔI_{th} (right y axis in linear scale) as a function of L.

TABLE III. Summary comparing the same laser parameters for a standard 1 mm and the selected 3 mm cavity length.

	Standard length (1 mm)	Optimized length (3 mm)
$\Delta\nu_{S-T}$	1	7.4×10^{-2}
ΔI_{th}	1	1.15

ΔI_{th} and $\Delta\nu_{S-T}$ are plotted in Fig. 10 as a function of L. $\Delta\nu_{S-T}$ in Fig. 10 (left y axis) exhibits an exponential decrease for longer cavities due to the larger total feedback κL, which reduces α_m. ΔI_{th}, reported in Fig. 10 (right y axis), does not have a monotonical relation with L. For L lower than an optimal value (around 1.4 mm), I_{th} reduces for longer cavities, similarly to the $\Delta\nu_{S-T}$ case, due to the shrinking of α_m. Instead, for cavities longer than 1.4 mm, I_{th} linearly increases with L. This is due to the effect of the L on the contact dimensions, represented by the factor $\frac{L_A}{L_0}$, which is dominant over the decrease in α_m for large L. A trade-off value for the L can be selected to achieve a consistent $\Delta\nu_{S-T}$ reduction but still retains a reasonable value for I_{th}. The trade-off L is chosen to be 3 mm, which reduces $\Delta\nu_{S-T}$ by a factor of 13.5, whereas I_{th} is inflated by 15% from the reference length of 1 mm; conversely, the optimal point for I_{th} is L = 1.4 mm, but this configuration only decrease $\Delta\nu_{S-T}$ by a factor of 1.8. A summary of the values for $\Delta\nu_{S-T}$ and ΔI_{th} is in Table III. L of 3 mm reduces the power density by a factor of 3 with respect to a reference 1 mm cavity. This decrease in power density will improve the laser output at high-power and extend its lifetime as this reduces the risk for COD and COMD.

IV. DFB LASER FABRICATION

The designed material epitaxial structure was grown using a metalorganic chemical-vapor deposition (MOCVD) reactor onto a GaAs substrate. Following material epitaxy, the sidewall Bragg grating and ridge waveguides were patterned using hydrogen silsesquioxane (HSQ) resist by electron beam lithography using a Raith EBPG 5200+ tool. The pattern was then transferred from the resist mask into the semiconductor material by RIE using an Oxford Instrument ICP180 tool with chlorine-based chemistry. The semiconductor grating was etched to just above the active region, as this reduces unwanted surface recombination and oxidation with the aim to mitigate COD and extend the device lifetime. The final etch depth was 1.5 μm with an aspect ratio ≥10. This entails a prominent RIE lagged etch rate in the sidewall grating recess demonstrated in Fig. 8, which motivated the consideration and correction for this non-ideal profile. The scanning electron microscopy (SEM) image of the sidewall Bragg grating after pattern transfer is shown in Fig. 11.

The sidewall Bragg structure was coated and planarized with spin-coating glass using HSQ resist, which assumes a glass-like structure, with a refractive index of 1.4, after thermal annealing above 180 °C, and then a plasma-enhanced chemical vapor deposition SiO_2 layer to passivate the structure. A narrow window was opened by RIE to the p-doped semiconductor side on top of the ridge. The sample was thinned to 250 μm by mechanical polishing to improve thermal heat sinking. A common Au-based negative back-contact and a patterned Au-based positive top-contact were deposited by metal evaporation. Finally, the laser cavity was generated by cleaving the sample in bars, which were then coated with antireflection (AR) and high-reflection (HR) coatings at the facet ends (R_{AR} < 0.1%/R_{HR} > 95%). Besides preventing oxidation of the facets (a major contributor to COMD[23]), the asymmetrical facet coating would allow for a better power extraction and prevent any Fabry–Pérot cavity feedback.

V. CHARACTERIZATION AND RESULTS

During characterization, the laser devices were mounted onto a brass mount to keep consistent operating conditions during continuous-wave emission. The brass mount acts as a common negative contact and heatsink, while a Peltier cooler maintained the heatsink constant at 15 °C.

The DFB laser was characterized for standard light-current–voltage (LIV) measurement to assess the behavior and P_{out} from the AR facet. Figure 12 reports the bias voltage and

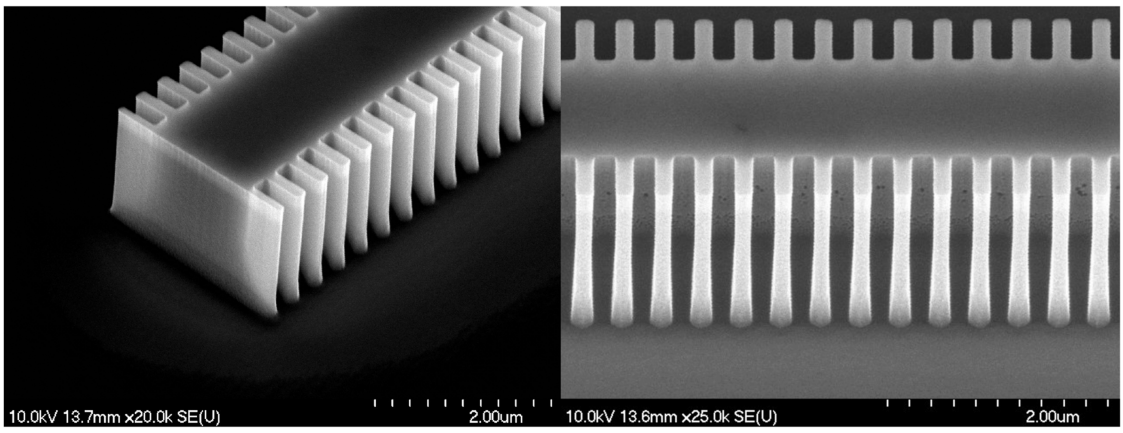

FIG. 11. SEM images of the sidewall Bragg grating after the pattern transfer into the semiconductor laser heterolayers.

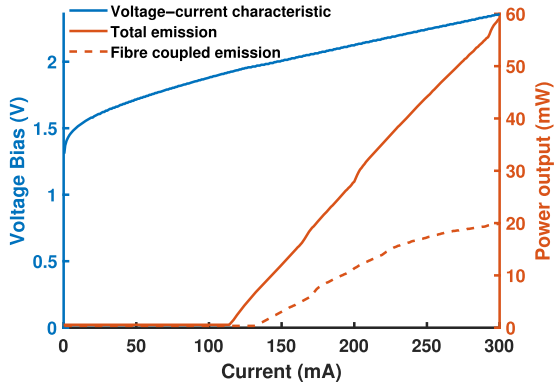

FIG. 12. The LIV measurement of the laser for both total and fiber-coupled power output.

P_{out} as a function of the injected current using a diode laser driver with 0.01 mA current steps and current noise ≤15 μA. P_{out} in Fig. 12 exhibits two curves; the higher curve is P_{out} collected by a large-area photodiode (i.e., <5 × 5 mm^2 in size); hence, it can be assumed that it is collecting the total emitted light from the AR facet. The lower curve reports the light coupled into a lensed single-mode fiber with 1.2 μm Gaussian beam waist and measured by using a fiber-coupled powermeter. The laser device exhibits a steady emission from I_{th} at 120 mA approaching a total P_{out} of 60 mW for 300 mA with a linear slope efficiency of 0.32 W/A. The laser current threshold of 120 mA results to be higher than standard DFB lasers, but it is compatible with the values reported for other devices in sidewall Bragg grating configuration in the literature.[24] The VI shows the correct diode characteristic and a device series resistance of 2.87 Ω. P_{out} coupled into a single-mode fiber (dotted line in Fig. 12) exhibits a coupling efficiency between 30% and 40% along the current sweep. This was expected as the fiber tip is aligned to the AR facet using a micro-manipulator stage at a fixed injection current of 240 mA. The thermal expansion (contraction) due to the increase (decrease) in current is sufficient to bring the two components out of the ideal alignment. Since both the laser facet and lensed fiber ends have a mode size in the order of 1–2 μm, the required alignment accuracy is of the same order. A number of DFB lasers, from the same fabrication of the laser reported in Fig. 12, were characterized with a maximum power range recorded between 40 and 60 mW and a coupling efficiency from 30% up to 50%, depending on the alignment conditions.

The fiber-coupled laser output was characterized by an optical spectrum analyzer, after passing through an in-fiber 60 dB isolator, which prevents unwanted feedback on the DFB laser. The measured emission spectra at different injection currents are reported in Fig. 13. The laser shows a stable and continuous single mode emission between I_{th} (120 mA) and the highest tested current (300 mA), except for a possible mode-hop between 180 and 200 mA, with a side-mode suppression ratio (SMSR) exceeding 35 dB in the considered current range. Moreover, the peak wavelength can be linearly tuned by current adjustment, mainly due to its effect on the p–i–n junction temperature, in a wavelength range ≥0.8 nm, which includes the target wavelength of 778.1 nm.

The far-field pattern emission from the AR-coated facet was measured and recorded, with particular attention to Θ. The far-field emission pattern was characterized by an automatic system with a mobile photodetector, which detects the power output as a function of the direction angle. The measured emission pattern was then normalized over the peak power and projected along the slow and fast axis, or horizontal and vertical directions, respectively. Figure 14 represents the projections of the far-field pattern in both horizontal and vertical directions alongside their simulated patterns, obtained from the Fourier transform of the ridge waveguide mode profile. The measured and simulated projections are in good agreement with the experimental FWHM Θ of 20.5°, which is only slightly larger than the simulated value of 19.7°. This narrower beam along the vertical direction justified the observed coupling efficiency with a lensed fiber of 40% in Fig. 12, a coupling improvement of 50% over

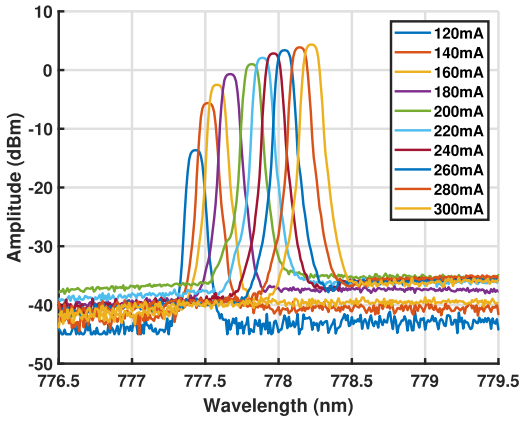

FIG. 13. The characterized optical spectrum of the DFB laser device. The device clearly shows a continuous tunable single-mode emission across the injection current range 120–300 mA, except for a possible mode-hop between 180 and 200 mA.

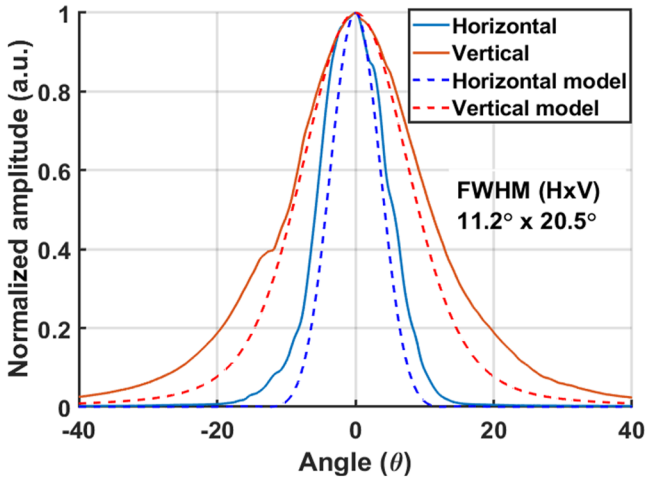

FIG. 14. The far-field emission pattern projected along the horizontal (blue) and the vertical (red) directions. The measured far-field projections (straight line) are compared with the simulated projection (dotted line).

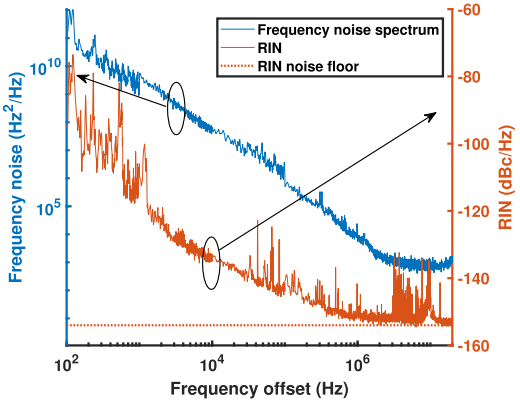

FIG. 15. The frequency noise spectrum as a function of the frequency noise (left y axis), measured at the emission wavelength of 778.1 nm (output power 47 mW at 15 °C). The Lorentzian linewidth, obtained from the white noise range, is 3.7 kHz. The RIN as a function of the frequency noise (right y axis). The RIN spectrum presents a plateau region of −154 dBc/Hz for frequency above 1 MHz, limited from the noise floor of the measurement (dotted line), which demonstrates the intrinsic low-noise DFB laser emission.

previous devices fabricated on material without the double-sided mode expander.[19] There is still a significant difference in profile between horizontal and vertical projections in Fig. 14. The far-field emission is still elliptical as the horizontal FWHM is almost half of the vertical FWHM, although the material optimization dramatically decreases the eccentricity of the ellipse.

The frequency noise and relative intensity noise (RIN) spectra were obtained using an OEWaves OE4000 noise measurement system, which employs a homodyne technique to characterize laser light coupled into its single mode fiber input. The Lorentzian laser linewidth was obtained from the white noise floor in the double-sided power spectral density, which for the frequency noise spectrum in Fig. 15 is extracted from the 1–10 MHz frequency range.[38]

In order to avoid any linewidth broadening or frequency noise from optical feedback, a 60 dB in-fiber optical isolator was included between the laser device and the noise measurement system. Figure 15 shows the recorded frequency noise and RIN as a function of the frequency at peak emission of 778.1 nm wavelength. Both spectra exhibit a higher noise level and multiple noise peaks for the low-frequency offset range. The higher low-frequency noise is expected for a free running laser device as it is affected by the current and thermal noise from the current driver and thermoelectric controller. This behavior is a consequence of the semiconductor properties where phase and amplitude noises are coupled;[33] this is physically due to the change in the semiconductor refractive index due to a change in either the injected current or temperature. Nevertheless, the instantaneous laser linewidth extracted from Fig. 15 achieves an extremely narrow value of 3.7 kHz, while the RIN shows an intrinsic noise level of −154 dBc/Hz, above 10 MHz frequency. The same frequency noise characterization was repeated

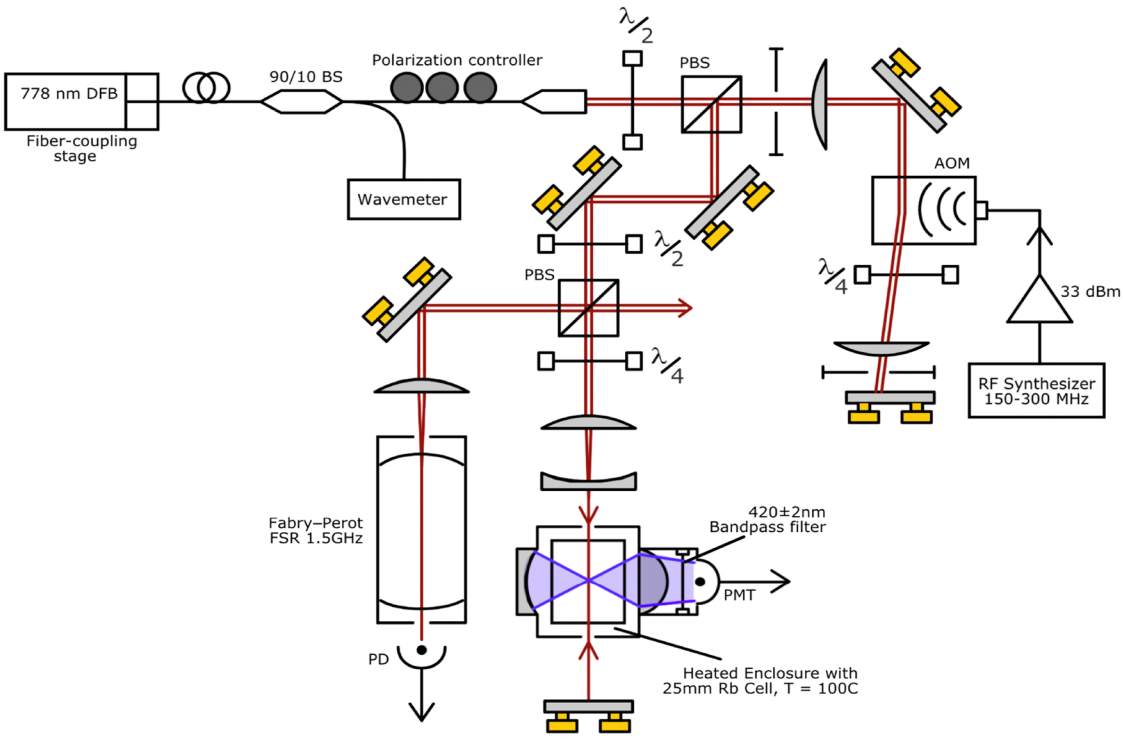

FIG. 16. The full measurement setup for TFT spectroscopy.

for multiple DFB lasers fabricated under the same conditions showing consistent intrinsic stability with Lorentzian linewidth between 3.7 and 7.5 kHz. These low noise levels indicate how the material and cavity optimizations have been successful in demonstrating the laser device at high operating power with intrinsic stability and narrow-linewidth emission.

VI. RUBIDIUM TWO-PHOTON SPECTROSCOPY

In order to demonstrate the benefit of the DFB laser's narrow linewidth with regard to quantum sensor applications, the laser was used to resolve the hyperfine levels of the ^{85}Rb and ^{87}Rb TPT. A single laser of 778.1 nm can be used to perform Doppler-free spectroscopy[39] in a heated vapor cell (110°) to excite the $5S_{1/2}$ (F = 2→) $5D_{5/2}(F' = 4)$ Rb TPT (see Fig. 1), providing a narrow signal of 334 kHz with modest signal-to-noise ratios through fluorescence detection at 420 nm.[12,13] The accessibility of such a narrow linewidth signal without requiring cooling of the atoms makes this reference transition highly lucrative for a compact optical clock.[5] The 3D diagram in Fig. 16 shows the setup used for doppler-free spectroscopy, including the use of a Hamamatsu H7827-002 photomultiplier tube (PMT) to detect the weak fluorescence signal of <1 nW at 420 nm. The TPT excites very weakly owing to the large detuning of ≃1 THz from the intermediate level of the two-photon excitation. A high pump intensity of 4 W/cm^2 is therefore required to provide a reasonable signal-to-noise ratio. This intensity was achieved delivering 6–7 mW from the DFB laser, which is then collimated into a 0.22 mm $1/e^2$ radius beam. Additionally, a 420 nm bandpass filter prevents scattered light at 778.1 nm from reaching the PMT and elevating the noise floor. Once the DFB laser is internally temperature- and current-tuned near the Rb TPT resonance, a scanning AOM then picks up a continuous scan of either the ^{87}Rb or ^{85}Rb hyperfine features at a rate of 3.3 GHz s^{-1}. Prior to spectroscopy, a small amount of laser power is directed to a Fabry–Pérot cavity, for checking the lasers mode is clean and stable during measurements. In the case of the ^{87}Rb TPT signal shown in Fig. 17, the linewidth was measured at ~0.8 MHz, with the majority of the linewidth attributed to the natural linewidth and an estimated transit-time broadening of 0.311 MHz.[40] Incomplete cancellation of background magnetic fields additionally increases the linewidth of this measurement, yet the analysis suggests that the DFB laser intrinsic linewidth is not adding a significant amount of noise to the measured linewidth and is capable of resolving a good signal at modest powers, i.e., <10 mW.

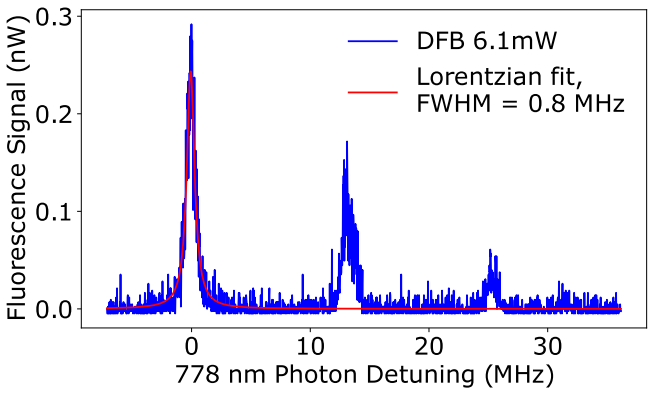

FIG. 17. The ^{87}Rb TPT spectrum using the free-running DFB laser.

TABLE IV. Size comparison between different lasers for atomic clock available. Although designed for different performance, the semiconductor DFB lasers offer a unique opportunity for size reduction and integrability on-chip.

	Standard clock laser	Benchtop laser	This work
Size (volume)	$> 5 \times 10^4$ mm^2	5×10^3 mm^2	<1 mm^2

Compared with other systems of similar design and purpose, previous work also demonstrates results of Doppler-free spectroscopy of the reference ^{87}Rb TPT using a 778 nm DFB laser.[14] Their results yielded a minimum TPT linewidth of 1.5–2 MHz while scanning their laser frequency at rates up to 463 GHz s^{-1}. More recent works achieved a measured linewidth of ~1 MHz using a Distributed Bragg Reflector (DBR) laser[5] and as narrow as 0.667 MHz on the ^{85}Rb TPT but using a stabilized external-cavity diode laser.[41]

VII. CONCLUSION

In summary, the DFB laser device characterization demonstrates a power emission of 58 mW at 300 mA, single-mode operation in the entire current range with a 0.8 nm tunability, and a Lorentzian linewidth of 3.7 kHz. Moreover, the emission pattern exhibits a more Gaussian-like beam profile with a vertical beam divergence of 20.5°, which translates into an improved coupling efficiency with lensed optical fiber ≥40%. This performance allowed the free-running DFB lasers to demonstrate spectroscopy of Rb vapor, which resolved the ^{85}Rb and ^{87}Rb TPTs, demonstrating a FWHM of 800 kHz limited by transit-time and magnetic broadening effects in the Rb vapor. In comparison to the standard lasers employed for atomic spectroscopy (see Table IV), the semiconductor DFB laser presented in this work opens the path for substantial miniaturization of optical atomic clock systems.

SUPPLEMENTARY MATERIAL

The supplementary material reports a comprehensive analysis and derivation for each of the laser parameters (Γ_{QW}, α_{loss}, Θ, κ, and $A_\perp$), considered in this work, as a function of the different configurations of the double-sided mode expander.

ACKNOWLEDGMENTS

This work was supported by the EPSRC (Project Nos. EP/N003225/1 and EP/T001046/1) and the Royal Academy of Engineering (Project No. CiET2021\123). The authors thank the staff of the James Watt Nanofabrication Centre for technical support during the fabrication of the devices.

AUTHOR DECLARATIONS

Conflict of Interest

The authors have no conflicts to disclose.

Author Contributions

E. Di Gaetano: Conceptualization (lead); Data curation (lead); Formal analysis (lead); Investigation (lead); Methodology (lead); Software (lead); Validation (lead); Visualization (lead); Writing – original draft (lead); Writing – review & editing (lead). **B. Keliehor**: Conceptualization (equal); Data curation (equal); Formal analysis (equal); Investigation (lead); Methodology (lead); Software (equal); Validation (equal); Visualization (equal); Writing – original draft (lead); Writing – review & editing (lead). **K. Gallacher**: Formal analysis (equal); Methodology (equal); Supervision (supporting); Validation (equal); Visualization (supporting); Writing – review & editing (equal). **P. F. Griffin**: Conceptualization (equal); Formal analysis (equal); Funding acquisition (equal); Project administration (equal); Resources (equal); Supervision (lead); Validation (equal); Writing – review & editing (equal). **M. Sorel**: Conceptualization (supporting); Funding acquisition (equal); Project administration (equal); Resources (equal); Supervision (equal); Validation (supporting); Writing – review & editing (equal). **E. Riis**: Conceptualization (equal); Formal analysis (equal); Funding acquisition (lead); Project administration (lead); Resources (equal); Supervision (lead); Validation (equal); Writing – review & editing (equal). **D. J. Paul**: Conceptualization (equal); Formal analysis (equal); Funding acquisition (lead); Project administration (lead); Resources (lead); Supervision (lead); Validation (equal); Writing – original draft (equal); Writing – review & editing (lead).

DATA AVAILABILITY

The data that support the findings of this study are available from the corresponding author upon reasonable request.

REFERENCES

[1] B. L. S. Marlow and D. R. Scherer, "A review of commercial and emerging atomic frequency standards," IEEE Trans. Ultrason. Ferroelectrics Freq. Control **68**, 2007–2022 (2021).

[2] U.K. Government Office for Science, "Satellite-derived time and position: A study of critical dependencies" (Government Office for Science, London, UK, 2018), https://assets.publishing.service.gov.uk/media/5a82c84ced915d74e34038ab/satellite-derived-time-and-position-blackett-review.pdf.

[3] S. Knappe, P. Schwindt, V. Shah, L. Hollberg, J. Kitching, L. Liew, and J. Moreland, "A chip-scale atomic clock based on ^{87}Rb with improved frequency stability," Opt. Express **13**, 1249–1253 (2005).

[4] A. D. Ludlow, M. M. Boyd, J. Ye, E. Peik, and P. O. Schmidt, "Optical atomic clocks," Rev. Mod. Phys. **87**, 637–701 (2015).

[5] Z. L. Newman, V. Maurice, T. Drake, J. R. Stone, T. C. Briles, D. T. Spencer, C. Fredrick, Q. Li, D. Westly, B. R. Ilic *et al.*, "Architecture for the photonic integration of an optical atomic clock," Optica **6**, 680–685 (2019).

[6] J. Kitching, "Chip-scale atomic devices," Appl. Phys. Rev. **5**, 031302 (2018).

[7] J. P. McGilligan, K. Gallacher, P. F. Griffin, D. J. Paul, A. S. Arnold, and E. Riis, "Micro-fabricated components for cold atom sensors," Rev. Sci. Instrum. **93**, 091101 (2022).

[8] T. Bothwell, D. Kedar, E. Oelker, J. M. Robinson, S. L. Bromley, W. L. Tew, J. Ye, and C. J. Kennedy, "JILA SrI optical lattice clock with uncertainty of 2.0×10^{-18}," Metrologia **56**, 065004 (2019).

[9] K. W. Martin, G. Phelps, N. D. Lemke, M. S. Bigelow, B. Stuhl, M. Wojcik, M. Holt, I. Coddington, M. W. Bishop, and J. H. Burke, "Compact optical atomic clock based on a two-photon transition in rubidium," Phys. Rev. Appl. **9**, 014019 (2018).

[10] V. Maurice, Z. L. Newman, S. Dickerson, M. Rivers, J. Hsiao, P. Greene, M. Mescher, J. Kitching, M. T. Hummon, and C. Johnson, "Miniaturized optical frequency reference for next-generation portable optical clocks," Opt. Express **28**, 24708–24720 (2020).

[11] S. Dyer, K. Gallacher, U. Hawley, A. Bregazzi, P. Griffin, A. Arnold, D. Paul, E. Riis, and J. McGilligan, "Chip-scale packages for a tunable wavelength reference and laser cooling platform," Phys. Rev. Appl. **19**, 044015 (2023).

[12] F. Nez, F. Biraben, R. Felder, and Y. Millerioux, "Optical frequency determination of the hyperfine components of the $5S_{12}$-$5D_{32}$ two-photon transitions in rubidium," Opt. Commun. **102**, 432–438 (1993).

[13] R. Felder, D. Touahri, O. Acef, L. Hilico, J.-J. Zondy, A. Clairon, B. de Beauvoir, F. Biraben, L. Julien, F. Nez, and Y. P. Millerioux, "Performance of a GaAlAs laser diode stabilized on a hyperfine component of two-photon transitions in rubidium at 778 nm," Proc. SPIE **2378**, 52–57 (1995).

[14] S. Kraft, A. Deninger, C. Trück, J. Fortágh, F. Lison, and C. Zimmermann, "Rubidium spectroscopy at 778–780 nm with a distributed feedback laser diode," Laser Phys. Lett. **2**, 71–76 (2005).

[15] S. Maeda, H. Morioka, H. Kumagai, and A. Kobayashi, "Conversion efficiency of 56% in frequency doubling of single-frequency coherent light from Ti:sapphire laser at 778 nm in high-finesse resonant cavity containing BiBO crystal," Nucl. Instrum. Methods Phys. Res., Sect. B **267**, 3471–3474 (2009).

[16] M. Poulin, C. Latrasse, N. Cyr, and M. Tetu, "An absolute frequency reference at 192.6 THz (1556 nm) based on a two-photon absorption line of rubidium at 778 nm for WDM communication systems," IEEE Photonics Technol. Lett. **9**, 1631–1633 (1997).

[17] C. S. Edwards, G. P. Barwood, H. S. Margolis, P. Gill, and W. R. C. Rowley, "Development and absolute frequency measurement of a pair of 778 nm two-photon rubidium standards," Metrologia **42**, 464 (2005).

[18] Y. Ding, G. Ternent, A. Saeed, C. J. Hamilton, N. Hempler, G. P. A. Malcolm, G. T. Maker, M. Sorel, and D. J. Paul, "GaAs-based distributed feedback laser at 780 nm for ^{87}Rb cold atom quantum technology," in *2017 European Conference on Lasers and Electro-Optics and European Quantum Electronics Conference* (Optical Society of America, 2017), p. CB-7-2.

[19] E. Di Gaetano, S. Watson, E. McBrearty, M. Sorel, and D. J. Paul, "Sub-megahertz linewidth 780.24 nm distributed feedback laser for ^{87}Rb applications," Opt. Lett. **45**, 3529–3532 (2020).

[20] K. Gallacher, M. Sinclair, R. W. Millar, O. Sharp, F. Mirando, G. Ternent, G. Mills, B. Casey, and D. J. Paul, "Integrated DFB lasers on Si_3N_4 photonic platform for chip-scale atomic systems," in *Conference on Lasers and Electro-Optics* (Optical Society of America, 2019), p. STu4O.7.

[21] K. Gallacher, P. F. Griffin, E. Riis, M. Sorel, and D. J. Paul, "Silicon nitride waveguide polarization rotator and polarization beam splitter for chip-scale atomic systems," APL Photonics **7**, 046101 (2022).

[22] A. Moser, "Thermodynamics of facet damage in cleaved AlGaAs lasers," Appl. Phys. Lett. **59**, 522–524 (1991).

[23] A. Moser and E. E. Latta, "Arrhenius parameters for the rate process leading to catastrophic damage of AlGaAs-GaAs laser facets," J. Appl. Phys. **71**, 4848–4853 (1992).

[24] H. Virtanen, T. Uusitalo, M. Karjalainen, S. Ranta, J. Viheriälä, and M. Dumitrescu, "Narrow-linewidth 780-nm DFB lasers fabricated using nanoimprint lithography," IEEE Photonics Technol. Lett. **30**, 51–54 (2018).

[25] T.-P. Nguyen, M. Schiemangk, S. Spießberger, H. Wenzel, A. Wicht, A. Peters, G. Erbert, and G. Tränkle, "Optimization of 780 nm DFB diode lasers for high-power narrow linewidth emission," Appl. Phys. B **108**, 767–771 (2012).

[26] T.-P. Nguyen, H. Wenzel, O. Brox, F. Bugge, P. Ressel, M. Schiemangk, A. Wicht, T. Quoc Tien, and G. Tränkle, "Spectral linewidth vs. front facet reflectivity of 780 nm DFB diode lasers at high optical output power," Appl. Sci. **8**, 1104 (2018).

[27] See https://www.lumerical.com/products/mode/ for information about the simulation software used to simulate the mode and far-field profiles reported.

[28]See https://www.nextnano.de/ for information about the simulation software used to model the materail active region.
[29]H. Fujii, Y. Ueno, and K. Endo, "Effect of thermal resistivity on the catastrophic optical damage power density of AlGaInP laser diodes," Appl. Phys. Lett. **62**, 2114–2115 (1993).
[30]J. Souto, J. L. Pura, and J. Jiménez, "Thermomechanical issues of high power laser diode catastrophic optical damage," J. Phys. D: Appl. Phys. **52**, 343002 (2019).
[31]E. A. Avrutin and B. S. Ryvkin, "Theory of direct and indirect effect of two-photon absorption on nonlinear optical losses in high power semiconductor lasers," Semicond. Sci. Technol. **32**, 015004 (2016).
[32]F. R. Gfeller and D. J. Webb, "Degradation and lifetime studies of high-power single-quantum-well AlGaAs ridge lasers," J. Appl. Phys. **68**, 14–20 (1990).
[33]C. Henry, "Theory of the linewidth of semiconductor lasers," IEEE J. Quantum Electron. **18**, 259–264 (1982).
[34]E. Di Gaetano and M. Sorel, "Design of chirped-coupling sidewall Bragg gratings for narrow linewidth distributed feedback lasers," Opt. Lett. **44**, 1642–1645 (2019).
[35]J. Buus, M.-C. Amann, and D. J. Blumenthal, "Single mode laser diodes," in *Tunable Laser Diodes and Related Optical Sources* (Wiley; IEEE Press, 2005), Chap. 3, pp. 43–78.
[36]P. Ilroy, A. Kurobe, and Y. Uematsu, "Analysis and application of theoretical gain curves to the design of multi-quantum-well lasers," IEEE J. Quantum Electron. **21**, 1958–1963 (1985).
[37]L. A. Coldren, S. W. Corzine, and M. L. Masanovic, "Mirrors and resonators for diode lasers," in *Diode Lasers and Photonic Integrated Circuits* (John Wiley and Sons, Ltd., 2012), Chap. **3**, pp. 91–155.
[38]G. Di Domenico, S. Schilt, and P. Thomann, "Simple approach to the relation between laser frequency noise and laser line shape," Appl. Opt. **49**, 4801–4807 (2010).
[39]G. Grynberg and B. Cagnac, "Doppler-free multiphotonic spectroscopy," Rep. Prog. Phys. **40**, 791 (1977).
[40]F. Biraben, M. Bassini, and B. Cagnac, "Line-shapes in Doppler-free two-photon spectroscopy. The effect of finite transit time," J. Phys. France **40**, 445–455 (1979).
[41]Z. L. Newman, V. Maurice, C. Fredrick, T. Fortier, H. Leopardi, L. Hollberg, S. A. Diddams, J. Kitching, and M. T. Hummon, "High-performance, compact optical standard," Opt. Lett. **46**, 4702–4705 (2021).